nature materials

LETTERS

https://doi.org/10.1038/s41563-021-00923-6

Imaging moiré flat bands in three-dimensional reconstructed WSe_2/WS_2 superlattices

Hongyuan Li[1,2,3,8], Shaowei Li[1,3,4,8] ✉, Mit H. Naik[1,3,8], Jingxu Xie[1], Xinyu Li[1], Jiayin Wang[1], Emma Regan[1,2,3], Danqing Wang[1,2], Wenyu Zhao[1], Sihan Zhao[1], Salman Kahn[1,3], Kentaro Yumigeta[5], Mark Blei[5], Takashi Taniguchi[6], Kenji Watanabe[7], Sefaattin Tongay[5], Alex Zettl[1,3,4], Steven G. Louie[1,3] ✉, Feng Wang[1,3,4] ✉ and Michael F. Crommie[1,3,4] ✉

Moiré superlattices in transition metal dichalcogenide (TMD) heterostructures can host novel correlated quantum phenomena due to the interplay of narrow moiré flat bands and strong, long-range Coulomb interactions[1–9]. However, microscopic knowledge of the atomically reconstructed moiré superlattice and resulting flat bands is still lacking, which is critical for fundamental understanding and control of the correlated moiré phenomena. Here we quantitatively study the moiré flat bands in three-dimensional (3D) reconstructed WSe_2/WS_2 moiré superlattices by comparing scanning tunnelling spectroscopy (STS) of high-quality exfoliated TMD heterostructure devices with ab initio simulations of TMD moiré superlattices. A strong 3D buckling reconstruction accompanied by large in-plane strain redistribution is identified in our WSe_2/WS_2 moiré heterostructures. STS imaging demonstrates that this results in a remarkably narrow and highly localized K-point moiré flat band at the valence band edge of the heterostructure. A series of moiré flat bands are observed at different energies that exhibit varying degrees of localization. Our observations contradict previous simplified theoretical models but agree quantitatively with ab initio simulations that fully capture the 3D structural reconstruction. Our results reveal that the strain redistribution and 3D buckling in TMD heterostructures dominate the effective moiré potential and the corresponding moiré flat bands at the Brillouin zone K points.

Moiré superlattices in two-dimensional (2D) heterostructures provide an attractive platform to explore novel correlated physics, since nearly flat electronic bands can be engineered to enhance the effects of electron–electron correlations. This was first seen in graphene-based moiré superlattices, where correlated insulator states, superconductivity and ferromagnetic Chern insulators have been observed in both twisted bilayer[6,9–12], double bilayer[7,13,14] and ABC trilayer[15–17] moiré systems. The TMD-based moiré superlattice can have even flatter minibands, thus enhancing the role of the long-range Coulomb interactions. They have recently emerged as a new model system to explore novel strongly correlated quantum phenomena, such as the correlated insulators and generalized Wigner crystal[1–5]. More exotic emerging states, such as charge transfer insulators and pair density waves, have been predicted to emerge from theoretical models of hole-doped WSe_2/WS_2 moiré heterostructures[18,19]. These correlated phenomena, however, depend sensitively on the precise structural and electronic properties of the underlying moiré superlattice, due to the delicate interplay amongst the atomic geometry, moiré band structure and Coulomb interactions. Fundamental understanding and quantum control of TMD-based moiré phenomena thus require both quantitative knowledge of three-dimensional (3D) superlattice reconstructions at the atomic level and flat band electronic structure at the meV energy level, something that has hitherto been missing.

Scanning tunnelling microscopy (STM) provides a powerful tool to characterize the atomic and electronic structure of moiré superlattices. Previous STM studies have successfully observed localized moiré flat bands and correlated electronic gaps in twisted bilayer graphene[20–23], and demonstrated moiré site-dependent electronic structure in TMD moiré superlattices[24–26]. Narrow moiré flat bands at the valence band edge of TMD heterostructures, however, have not yet been reported. Part of the challenge is the difficulty in fabricating high-quality exfoliated TMD moiré heterostructures on insulating substrates that are suitable for STM characterization. As a result, previous STM studies often focused on chemical vapour deposition (CVD) grown TMD heterostructures on conducting graphite. CVD growth, however, yields lower sample quality and very limited control of stacking order and twist angle of the TMD heterostructure compared to exfoliation and stacking techniques. A graphite substrate can also pin the Fermi level of the TMD material and induce undesirable electronic screening and modification of TMD band structure[27–29].

In this work we determine the moiré flat band electronic structure of 3D reconstructed WSe_2/WS_2 moiré superlattices by combining scanning tunnelling spectroscopy (STS) of high-quality exfoliated TMD heterostructure devices with ab initio simulations of both the atomic geometry and electronic band structure of TMD moiré superlattices. Our STM imaging and theoretical simulations reveal a striking 3D buckling reconstruction of the WS_2/WSe_2 heterostructures that is accompanied by strong strain redistribution

[1]Department of Physics, University of California at Berkeley, Berkeley, CA, USA. [2]Graduate Group in Applied Science and Technology, University of California at Berkeley, Berkeley, CA, USA. [3]Materials Sciences Division, Lawrence Berkeley National Laboratory, Berkeley, CA, USA. [4]Kavli Energy Nano Sciences Institute at the University of California Berkeley and the Lawrence Berkeley National Laboratory, Berkeley, CA, USA. [5]School for Engineering of Matter, Transport and Energy, Arizona State University, Tempe, AZ, USA. [6]International Center for Materials Nanoarchitectonics, National Institute for Materials Science, Tsukuba, Japan. [7]Research Center for Functional Materials, National Institute for Materials Science, Tsukuba, Japan. [8]These authors contributed equally: Hongyuan Li, Shaowei Li, Mit H. Naik. ✉e-mail: swli@berkeley.edu; sglouie@berkeley.edu; fengwang76@berkeley.edu; crommie@physics.berkeley.edu

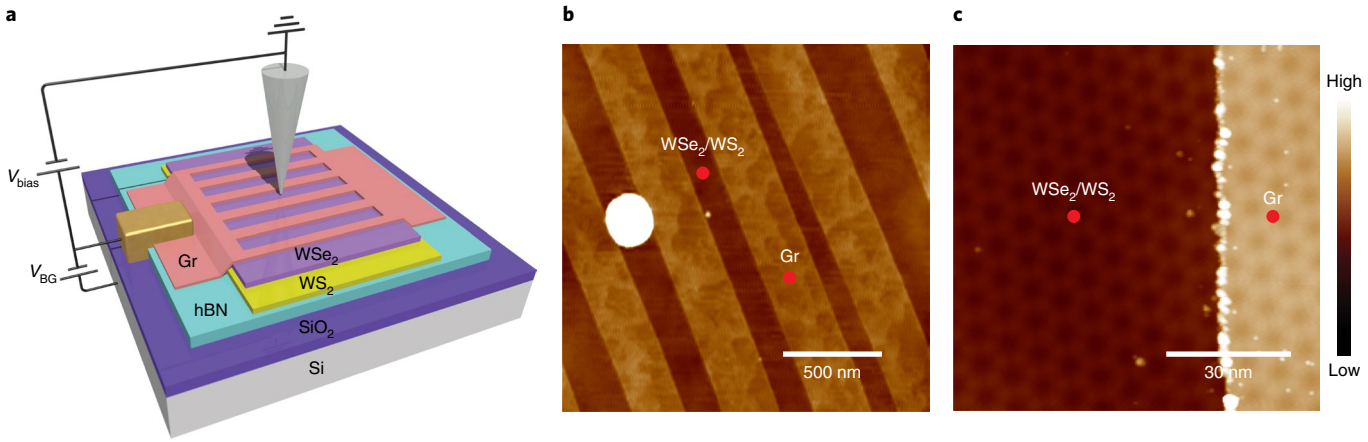

Fig. 1 | Aligned WSe_2/WS_2 heterostructure. a, Schematic of gate-tuneable WSe_2/WS_2 heterostructure device used for STM study. Graphene nanoribbons (Gr) are placed on top of the WSe_2/WS_2 as contact electrodes. **b**, Room-temperature ambient atomic force microscopy image of the sample surface. Exposed WSe_2/WS_2 and graphene-covered areas are labelled. **c**, Ultrahigh vacuum STM image of the exposed WSe_2/WS_2 and graphene-covered area ($T = 5.4$ K). A moiré superlattice can be seen clearly in both areas. $V_{bias} = -3$ V, $I = 100$ pA.

within the moiré superlattice. We observe multiple moiré flat bands at the valence band edge that originate from the K point, as well as a separate set of deep-lying moiré flat bands that originate from the Γ point (our convention is to refer to the K and Γ points of the unfolded WSe_2 Brillouin zone (BZ) instead of the moiré BZ). The topmost valence flat band from the K point is prominently narrow with a width of only 10 meV, and is expected to be responsible for the recently observed novel correlated insulator behaviour and generalized Wigner crystal states[1,3–5]. The strong localization of this band at the $B^{Se/W}$ stacking site revealed by STS spatial mapping contradicts previous simplified density functional theory (DFT) calculations, which predict localization at the AA site[18,19,24,25]. The STS results, however, are fully consistent with our DFT results obtained using a calculated large 3D reconstructed moiré superlattice. Our results show that the unexpected 3D moiré reconstruction and strain redistribution play a dominant role in determining the lowest energy moiré flat bands in WS_2/WSe_2 heterostructures.

The schematic of our WSe_2/WS_2 heterostructure device is shown in Fig. 1a. We used an array of graphene nanoribbons (GNRs) as contact electrodes, and the silicon substrate as a back gate to control the carrier density of the heterostructure. Details of the device fabrication are presented in the Supplementary Information. Figure 1b shows an ambient atomic force microscopy image of the top surface of the device: an array of GNRs (each separated by 100 to ~200 nm) partially covers the WSe_2/WS_2 heterostructure. Figure 1c shows an enlarged large-scale ultrahigh vacuum STM image of the heterostructure. The moiré superlattice can be clearly resolved in both the exposed TMD and GNR-covered areas, demonstrating the high quality of the heterostructure device.

Figure 2a shows a zoomed-in STM image of the moiré superlattice in the exposed TMD area. It shows a moiré period of 8.16 nm, which is consistent with the period expected for an aligned WSe_2/WS_2 heterostructure with a near-zero twist angle. Importantly, the heterostructure shows large height variation at different sites within a moiré unit cell, resulting in an overall honeycomb lattice characterized by a large valley at each hexagon centre that is surrounded by six peaks. The apparent height variation in an STM image always results from a convolution of geometric height change and electronic local density of states (LDOS) change, making it difficult to determine 'true' height variation via STM. To eliminate this complication, we exploited the graphene-covered TMD region, where the thin graphene layer covers the moiré superlattice conformally, but the electronic LDOS of graphene remains nearly constant. Figure 2b displays an STM topography image of the moiré superlattice in the graphene-covered area using a bias of −0.19 V. This bias lies within the TMD gap, and so all of the tunnelling current flows through the graphene layer. The similarity between Fig. 2a,b confirms that the WSe_2/WS_2 topographical landscape does, in fact, feature six peaks surrounding one valley.

The moiré superlattice is formed by a periodic change in the layer stacking configurations between the top WSe_2 and the bottom WS_2 layers. Three high-symmetry stacking configurations are illustrated in Fig. 2d, and denoted as the $B^{W/S}$, $B^{Se/W}$ and AA stackings, respectively. $B^{W/S}$ and $B^{Se/W}$ correspond to AB stackings. A common explanation for height modulation in TMD heterostructures is the stacking-dependent layer separation: the AA stacking has the largest interlayer spacing due to steric hindrance from the overlap of Se atoms in the WSe_2 layer and S atoms in the WS_2 layer, while the $B^{Se/W}$ and $B^{W/S}$ stacking sites have smaller interlayer separations. To better understand the structural reconstruction of the moiré pattern, we first carried out a force field-based simulation of the superlattice. Figure 2c shows the resulting interlayer spacing distribution in a vertical-only, relaxed, freestanding simulated WS_2/WSe_2 superlattice, which indeed exhibits a peak at the AA stacking site. This stacking-dependent layer separation, however, does not explain our experimental data, since it predicts a peak (AA) surrounded by six valleys ($B^{W/S}$ and $B^{Se/W}$), exactly the opposite of the STM images shown in Fig. 2a,b.

To account for our experimental observations, we must consider additional 3D reconstruction of the moiré heterostructure. Recent studies have suggested that 3D reconstruction of TMD moiré superlattices may be significant[30], but there have been no ab initio simulations of this effect. Our ab initio simulations of the WSe_2/WS_2 heterostructure reveal a strong moiré superlattice reconstruction that includes both a large in-plane strain distribution and a prominent out-of-plane buckling. Figure 2e shows the calculated in-plane strain distribution within the WSe_2 layer of the heterostructure. The heterostructure tends to increase the area of the interlayer-locked AB stacking regions due to its lower energy than AA stacking. As a result, the WSe_2 layer becomes locally compressed at the AB stacking regions due to its larger lattice constant compared with WS_2. The residual tensile strain localizes to the AA stacking region (Fig. 2e). The WS_2, with smaller lattice constant, has the opposite strain distribution (Supplementary Fig. 7). To partially release this strain, the heterobilayer reconstructs in three dimensions by an in-phase buckling in the out-of-plane direction (Fig. 2h,i). The simulated height distribution of the top WSe_2 layer (Fig. 2f) perfectly

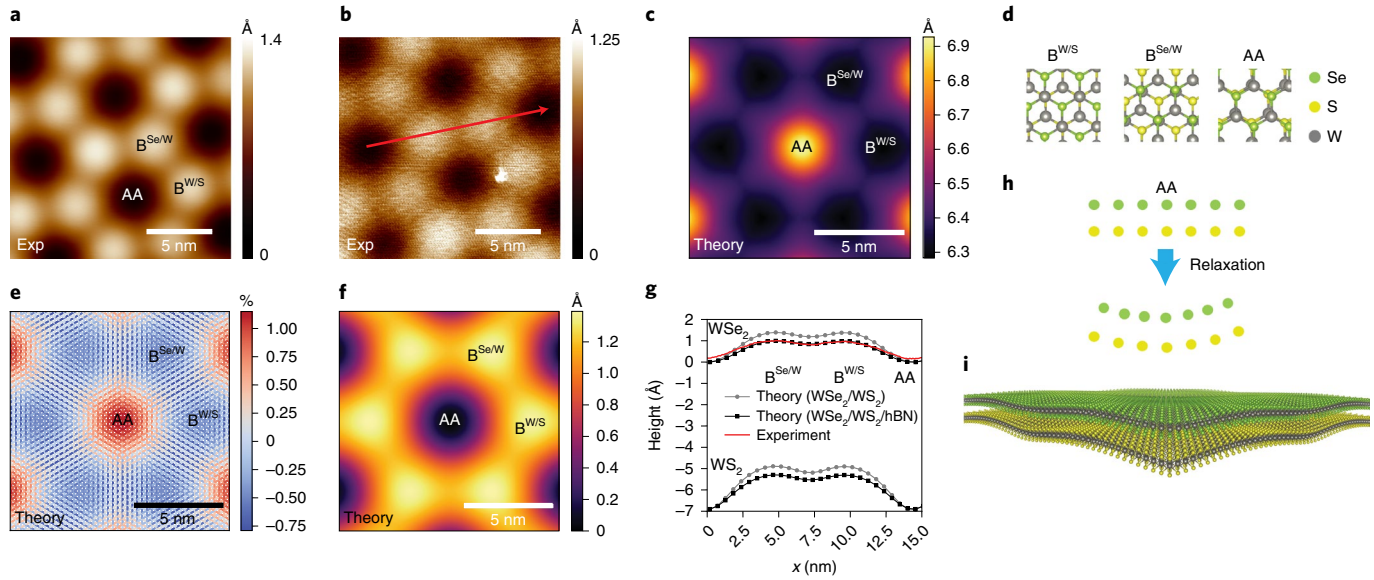

Fig. 2 | Moiré superlattice reconstruction. a, STM image of the exposed WSe_2/WS_2 area shows a moiré period of ~8 nm ($V_{bias} = -3$ V, $I = 100$ pA). **b**, STM image of the graphene-covered area ($V_{bias} = -0.19$ V, $I = 100$ pA). The STM image here better reflects the true topography of the heterostructure (see text). **c**, Theoretical interlayer spacing distribution from simulation. **d**, Schematic of the three types of stacking: $B^{W/S}$, $B^{Se/W}$ and AA. **e**, Theoretical in-plane strain distribution (in %) for the WSe_2 layer from simulation. **f**, Theoretical height profile of the W atoms in the top WSe_2 layer from simulation. **g**, Calculated 3D buckling of the heterostructure and comparison to experiment. Black and grey dots show the simulated positions of W atoms for a freestanding heterostructure and a heterostructure supported by hBN, respectively. Red trace shows the experimental line-cut from **b**. **h**, Schematic of the buckling process. **i**, 3D view of the reconstructed WSe_2/WS_2 moiré superlattice from simulation. Exp, experiment.

reproduces our STM image (Fig. 2a,b). Figure 2g shows a side view of the 3D reconstructed heterostructure from both experiment and theory. The buckling above the AA 'valley' causes the AB sites to rise. It is noteworthy that the presence of an hexagonal BN (hBN) substrate only slightly reduces the buckling effect (see Supplementary Information for more details). The simulated line profile agrees well with our experimental data (Fig. 2g).

The moiré superlattice reconstruction has a profound impact on the electronic properties of the moiré flat bands. To observe this effect, we used STS to probe the local electronic structure of the WSe_2/WS_2 heterostructure. Figure 3a displays the STS dI/dV spectra acquired at different moiré sites for $-3\,V < V_{Bias} < 2\,V$. Differences are seen in the spectra obtained at different moiré sites, which are consistent with previous studies performed on bilayer heterostructures grown on graphite[21,22].

We first focus our analysis of the STS spectra on the moiré flat band closest to the valence band edge, where the effects of strongly correlated states have been observed previously[1,4,5]. A challenge in the STM study of TMD materials is how to distinguish electronic states arising from K or Γ points in the single-layer BZ[21,22]. Here we utilize two distinct features of the K-point states to identify them. We first use the fact that, due to the much larger in-plane momentum of K-point states, their wavefunction decays faster outside the TMD layer (see details in the Supplementary Information). Figure 3b shows the height-dependent dI/dV spectra measured at one of the AB sites (ultimately confirmed as a $B^{Se/W}$ site) in the moiré pattern. Two prominent peaks are observed near $V_{bias} = -1.7$ V and $V_{bias} = -1.5$ V. The peak near −1.5 V exhibits a much stronger height dependence than the peak near −1.7 V, suggesting that the peaks at −1.5 V and −1.7 V correspond to electronic states at the K and Γ points, respectively. We next use the two facts that the TMD K-point electron wavefunctions have large in-plane momentum and are mainly contributed by the W d orbital with angular momentum $m = \pm 2$, which will induce atomic-scale alternating constructive and destructive interference patterns as illustrated in Fig. 3d (see details in Supplementary Information). The high-resolution dI/dV mapping at −1.5 V shows pronounced dI/dV signal oscillation over atomic-scale distances that match the WSe_2 lattice (Fig. 3e), while the dI/dV mapping at −1.7 V varies more smoothly (Fig. 3f). This behaviour confirms that the −1.5 V peak originates from K-point states at the valence band edge, whereas the −1.7 V peak originates from Γ-point states.

We performed larger scale dI/dV mapping to directly visualize the localization of the flat bands in real space. Figure 3g,i shows dI/dV maps obtained at the two peak energies −1.52 V (labelled K1) and −1.73 V (labelled Γ1). The LDOS for both of these flat band states are found to be strongly localized at the $B^{Se/W}$ site. Atomic-scale site dependence in the dI/dV signal for K-point states is again reflected in the K1 dI/dV mapping. Figure 3h,j shows the dI/dV mapping at slightly lower energies. The LDOS distribution is seen to change dramatically and now shows LDOS minima, where previously there were maxima at the $B^{Se/W}$ site.

To better determine the energy-dependent LDOS of the moiré flat bands, Fig. 3k shows a density plot of dI/dV spectra for the bias range $-1.72\,V < V_{bias} < -1.42\,V$ along the $B^{W/S}$–$B^{Se/W}$–AA direction, indicated by the yellow path marked in Fig. 3g. Figure 3l shows the same plot, but over a different bias range: $-1.86\,V < V_{bias} < -1.63\,V$. Figure 3k shows a prominent moiré flat band at the valence band minimum that is strongly localized at the $B^{Se/W}$ site. This K-point moiré flat band is isolated from deeper moiré flat bands by a gap of ~50 meV. Figure 3c displays a high-resolution dI/dV spectrum at the $B^{Se/W}$ site, which exhibits a peak having a full width at half maximum (FWHM) of 12 mV ± 1 mV. After a deconvolution eliminating the impact of the modulation voltage, the FWHM of the dI/dV peak is 10 mV ± 1 mV (see Supplementary Information for details), which sets an upper limit on the bandwidth of the moiré flat band of WSe_2/WS_2. The occupied moiré miniband in twisted bilayer graphene, by comparison, has an experimental bandwidth of 10 to ~40 meV (refs. [17–20]). The narrowness of the WSe_2/WS_2 moiré flat band in combination with the strong long-range Coulomb interactions in 2D

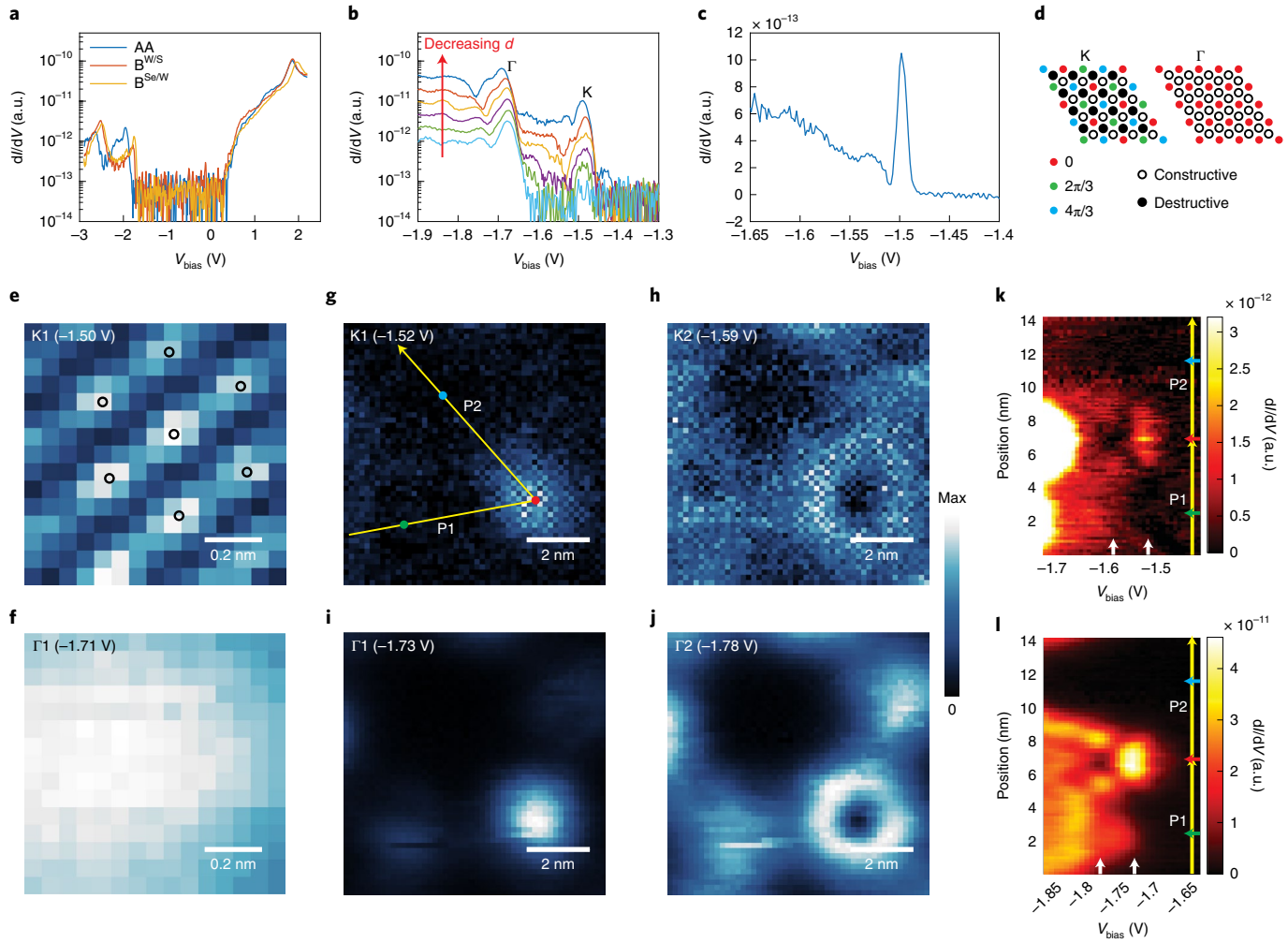

Fig. 3 | STS measurement of moiré-induced flat bands. a, Moiré site-dependent d*I*/d*V* spectra with low current set point ($V_{bias}=-3$ V, $I=70$ pA). Peaks in the $-2\,V<V_{bias}<-1.7$ V range show strong moiré site-dependent peak positions. **b**, Tip–sample distance (*d*)-dependent STS at the $B^{Se/W}$ site ($V_{bias}=-2.15$ V, $I=50, 100, 200, 400, 800, 1{,}600$ pA). A second peak near $V_{bias}=-1.5$ V emerges with decreased *d*, indicating that it has a larger decay constant and originates from K-point states. **c**, High-resolution d*I*/d*V* spectrum measured at the $B^{Se/W}$ site. A sharp peak with FWHM of 12 mV ± 1 mV can be observed near $V_{bias}=-1.5$ V (uncertainty in the FWHM of this peak comes from the standard deviation of widths extracted from spectra obtained at different $B^{Se/W}$ sites). **d**, Illustration of the atomic-scale wavefunction interference pattern. K-point states have a 2π phase winding over the adjacent three W atoms, while Γ-point states have identical phases over all Se atom sites. **e**,**f**, High-resolution d*I*/d*V* mappings measured at the same $B^{Se/W}$ region with biases corresponding to the K-point (−1.50 V) (**e**) and the Γ-point (−1.71 V) (**f**) peaks. Black hollow circles in **e** show the atomic-scale constructive interference points as illustrated in **d**. **g**,**h**, Large-scale d*I*/d*V* mappings of K-point states for $V_{bias}=-1.52$ V (**g**) and $V_{bias}=-1.59$ V (**h**). **i**,**j**, Large-scale d*I*/d*V* mappings and Γ-point states for $V_{bias}=-1.73$ V (**i**) and $V_{bias}=-1.78$ V (**j**). Panels **g**–**j** show the same region of the sample surface. Solid dots in **g** label the positions of $B^{Se/W}$ (red), $B^{W/S}$ (green) and AA (blue) sites. **k**,**l**, d*I*/d*V* density plot of K-point (**k**) and Γ-point (**l**) states along the two-segment yellow path shown in **g**. The corresponding path is also shown in **k**,**l**. Horizontal arrows label the positions of the $B^{W/S}$ (green), $B^{Se/W}$ (red) and AA (blue) sites. White vertical arrows label the energies used in **g**–**j**. $V_{BG}=50$ V for all measurements shown. The tip–sample distance is determined by the set point $V_{bias}=-2.15$ V, $I=800$ pA for all spectroscopy shown. The lock-in modulation is 20 mV for all panels except **c**, where the lock-in modulation is 5 mV.

semiconductors[24] makes this TMD heterostructure an excellent platform to explore highly correlated quantum phenomena.

In addition to the valence band edge moiré flat band, Fig. 3k shows that deeper moiré flat bands having different wavefunction spatial characteristics are present, but these bands are not well isolated. One such flat band can be tentatively identified near −1.6 V in Fig. 3h. The d*I*/d*V* map of this flat band (labelled K2) shows a ring around the centre of the $B^{Se/W}$ site and a weak plateau at the $B^{W/S}$ site. The ring-shaped electron wavefunction around the $B^{Se/W}$ site is reminiscent of the first excited states of a harmonic oscillator for a potential well centred on this site.

Figure 3l shows deeper flat bands mostly originating from the Γ point. The Γ-point moiré flat band closest to the valence band edge lies at −1.73 V and is localized to the $B^{Se/W}$ site. At the slightly deeper energy of −1.78 V a new wavefunction distribution is seen and the LDOS now shows a minimum at the $B^{Se/W}$ site (Fig. 3j). The ring-shaped electron wavefunction around the $B^{Se/W}$ site in this case is once again reminiscent of the first excited states of a harmonic oscillator (additional d*I*/d*V* mapping and position-dependent d*I*/d*V* spectra are included in the Supplementary Information).

To interpret the observed moiré minibands, we performed large-scale DFT calculations on the force field-reconstructed moiré superlattice. Figure 4a shows the calculated valence band structure for the WSe_2/WS_2 moiré superlattice in the mini-BZ (left) and the corresponding plot of the density of states (DOS) (right). The valence band edge is set at $E=0$. The bands closest to the valence band edge

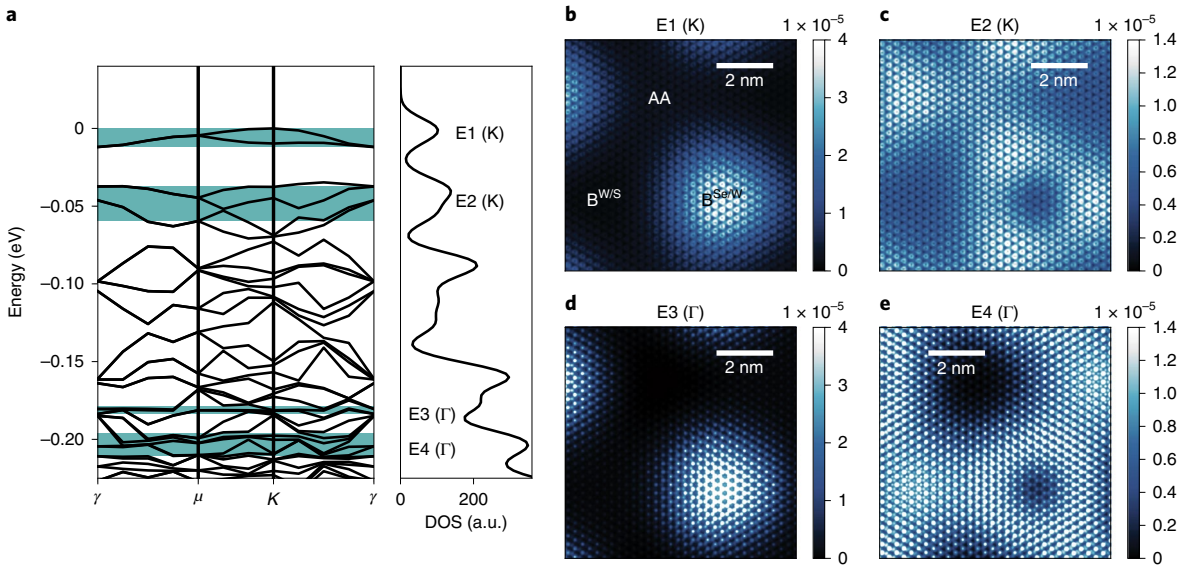

Fig. 4 | Ab initio calculations of the electronic structure in reconstructed moiré superlattice. a, Calculated electronic band structure plotted in the folded mini-BZ (left) and the corresponding plot of the DOS with 10 meV Gaussian broadening (right). Four important energy ranges (E1–E4) are labelled (green shaded areas) to highlight the topmost states folded from the K point (E1, E2) and Γ point (E3, E4). **b**–**e**, Calculated LDOS maps over a patch of area corresponding to the region used for d*I*/d*V* maps in Fig. 3g–i. The LDOS maps are averaged over different energy ranges as labelled in **a**: E1, originating from K point (**b**); E2, originating from K point (**c**); E3, originating from Γ point (**d**); and E4, originating from Γ point (**e**). The maps are also averaged over the out-of-plane direction.

(0, to approximately −0.18 eV) are folded from the K point, whereas the deeper bands below −0.18 eV have mixed origins from both the K point and the Γ point. Their origins can be distinguished by their LDOS distributions in the out-of-plane direction (see detailed discussion in the Supplementary Information). We labelled four important energy ranges (E1–E4) in Fig. 4a. The topmost valence band (within E1) has a bandwidth of only ~10 meV and is separated from the next band (within E2) by ~30 meV. The narrow, energetically isolated nature of the topmost band is in quantitative agreement with our experimental observations (Fig. 3c). The deeper bands tend to mix with each other and are thus hard to distinguish experimentally. The topmost bands folded from the Γ point are within E3, while the next set of deeper bands are within E4. The states in the gap between E3 and E4 are folded from the K point.

The spatial distribution of the calculated charge density for the flat band states agrees well with the STS results. Figure 4b–e shows the calculated LDOS distribution averaged over the four different energy ranges E1–E4, as well as averaged over the out-of-plane direction. Figure 4b shows the calculated LDOS for E1, mainly the topmost flat band from the K point. The LDOS is observed to localize strongly in the $B^{Se/W}$ region of the moiré unit cell. This matches the experimental behaviour quite well (Fig. 3g), and, in fact, allows us to distinguish the $B^{Se/W}$ region from the $B^{S/W}$ region in our experimental images. As we move deeper into the valence bands (E2) our simulation reveals a delocalization of the K-point LDOS and the formation of a node at the centre of the $B^{Se/W}$ region (Fig. 4c). This closely matches our experimental observations (Fig. 3h). The Γ-point LDOS behaves similarly, as seen by the comparison of theoretical Fig. 4d,e with experimental Fig. 3i,j. Once again we see the topmost Γ-point states (E3) showing strong localization in the $B^{Se/W}$ region, as well as increased delocalization accompanied by the formation of a node at slightly deeper energies (E4). The calculated energy separation between the topmost K and the Γ states (180 ± 20 meV between E1 and E3) is also very similar to the experimental energy separation between the K1 and Γ1 states (205 ± 1 meV). We thus observe very reasonable agreement between experiment and theory for both the flat band energy separation and the flat band spatial LDOS distribution.

It is conventionally believed that the interlayer interaction variation is the dominant effect in modulating the electronic structure of moiré superlattices[2]. However, our DFT calculation reveals that the flat bands at the K point are mainly a result of the deformation of the monolayer, instead of a hybridization-induced interlayer potential. Similar K -point flat band behaviour can be reproduced by calculating the electronic structure of a puckered monolayer WSe_2 extracted from the relaxed moiré superlattice (Supplementary Fig. 10). The Γ-point flat bands, on the other hand, do arise from inhomogeneous interlayer hybridization within the moiré superlattice. Additional discussion regarding the origin of the flat band localization is presented in the Supplementary Information.

In summary, we find that 3D moiré reconstruction dominates the low-energy moiré electronic structure, resulting in a narrow moiré flat band with 10 meV bandwidth at the valence band maximum in WS_2/WSe_2 heterostructures. Such quantitative understanding of the atomic and electronic structure within a moiré superlattice is crucial for simulating the Hubbard model and for the future control of novel correlated phenomena in TMD-based moiré heterostructures.

Online content

Any methods, additional references, Nature Research reporting summaries, source data, extended data, supplementary information, acknowledgements, peer review information; details of author contributions and competing interests; and statements of data and code availability are available at https://doi.org/10.1038/s41563-021-00923-6.

Received: 27 August 2020; Accepted: 7 January 2021;
Published online: 8 February 2021

References

1. Tang, Y. et al. Simulation of Hubbard model physics in WSe_2/WS_2 moiré superlattices. *Nature* **579**, 353–358 (2020).

2. Wu, F., Lovorn, T., Tutuc, E. & MacDonald, A. H. Hubbard model physics in transition metal dichalcogenide moiré bands. *Phys. Rev. Lett.* **121**, 026402 (2018).
3. Shimazaki, Y. et al. Strongly correlated electrons and hybrid excitons in a moiré heterostructure. *Nature* **580**, 472–477 (2020).
4. Regan, E. C. et al. Mott and generalized Wigner crystal states in WSe_2/WS_2 moiré superlattices. *Nature* **579**, 359–363 (2020).
5. Wang, L. et al. Correlated electronic phases in twisted bilayer transition metal dichalcogenides. *Nat. Mater.* **19**, 861–866 (2020).
6. Yankowitz, M. et al. Tuning superconductivity in twisted bilayer graphene. *Science* **363**, 1059–1064 (2019).
7. Liu, X. et al. Tunable spin-polarized correlated states in twisted double bilayer graphene. *Nature* **583**, 221–225 (2020).
8. Kim, K. et al. Tunable moiré bands and strong correlations in small-twist-angle bilayer graphene. *Proc. Natl Acad. Sci. USA* **114**, 3364–3369 (2017).
9. Lu, X. et al. Superconductors, orbital magnets and correlated states in magic-angle bilayer graphene. *Nature* **574**, 653–657 (2019).
10. Cao, Y. et al. Correlated insulator behaviour at half-filling in magic-angle graphene superlattices. *Nature* **556**, 80–84 (2018).
11. Cao, Y. et al. Unconventional superconductivity in magic-angle graphene superlattices. *Nature* **556**, 43–50 (2018).
12. Zondiner, U. et al. Cascade of phase transitions and Dirac revivals in magic-angle graphene. *Nature* **582**, 203–208 (2020).
13. Burg, G. W. et al. Correlated insulating states in twisted double bilayer graphene. *Phys. Rev. Lett.* **123**, 197702 (2019).
14. Cao, Y. et al. Tunable correlated states and spin-polarized phases in twisted bilayer–bilayer graphene. *Nature* **583**, 215–220 (2020).
15. Chen, G. et al. Evidence of a gate-tunable Mott insulator in a trilayer graphene moiré superlattice. *Nat. Phys.* **15**, 237–241 (2019).
16. Chen, G. et al. Tunable correlated Chern insulator and ferromagnetism in a moiré superlattice. *Nature* **579**, 56–61 (2020).
17. Chen, G. et al. Signatures of tunable superconductivity in a trilayer graphene moiré superlattice. *Nature* **572**, 215–219 (2019).
18. Slagle, K. & Fu, L. Charge transfer excitations, pair density waves, and superconductivity in moiré materials. *Phys. Rev. B* **102**, 235423 (2020).
19. Zhang, Y., Yuan, N. F. & Fu, L. Moiré quantum chemistry: charge transfer in transition metal dichalcogenide superlattices. *Phys. Rev. B* **102**, 201115 (2020).
20. Kerelsky, A. et al. Maximized electron interactions at the magic angle in twisted bilayer graphene. *Nature* **572**, 95–100 (2019).
21. Xie, Y. et al. Spectroscopic signatures of many-body correlations in magic-angle twisted bilayer graphene. *Nature* **572**, 101–105 (2019).
22. Jiang, Y. et al. Charge order and broken rotational symmetry in magic-angle twisted bilayer graphene. *Nature* **573**, 91–95 (2019).
23. Choi, Y. et al. Electronic correlations in twisted bilayer graphene near the magic angle. *Nat. Phys.* **15**, 1174–1180 (2019).
24. Pan, Y. et al. Quantum-confined electronic states arising from the moiré pattern of MoS_2–WSe_2 heterobilayers. *Nano Lett.* **18**, 1849–1855 (2018).
25. Zhang, C. et al. Interlayer couplings, moiré patterns, and 2D electronic superlattices in MoS_2/WSe_2 hetero-bilayers. *Sci. Adv.* **3**, e1601459 (2017).
26. Zhang, Z. et al. Flat bands in twisted bilayer transition metal dichalcogenides. *Nat. Phys.* **16**, 1093–1096 (2020).
27. Raja, A. et al. Coulomb engineering of the bandgap and excitons in two-dimensional materials. *Nat. Commun.* **8**, 15251 (2017).
28. Wang, G. et al. Colloquium: excitons in atomically thin transition metal dichalcogenides. *Rev. Mod. Phys.* **90**, 021001 (2018).
29. Ugeda, M. M. et al. Giant bandgap renormalization and excitonic effects in a monolayer transition metal dichalcogenide semiconductor. *Nat. Mater.* **13**, 1091–1095 (2014).
30. Waters, D. et al. Flat bands and mechanical deformation effects in the moiré superlattice of MoS_2-WSe_2 heterobilayers. *ACS Nano* **14**, 7564–7573 (2020).

Data availability

The data supporting the findings of this study are included in the main text and in the Supplementary Information files, and are also available at https://github.com/HongyuanLiCMP/Moire_STM_source_data.

Acknowledgements

This work was supported by the Director, Office of Science, Office of Basic Energy Sciences, Materials Sciences and Engineering Division of the US Department of Energy under the van der Waals heterostructure program (KCWF16), contract number DE-AC02-05CH11231 (device electrode preparation, STM spectroscopy, DFT calculations and theoretical analysis). Support was also provided by the US Army Research Office under MURI award W911NF-17-1-0312 (device layer transfer), and by the National Science Foundation Awards DMR-1807233 (surface preparation) and DMR-1926004 (GW calculations). S.T. acknowledges support from DOE-SC0020653, NSF DMR 1552220, DMR 1904716 and NSF CMMI 1933214 for WSe_2 and WS_2 bulk crystal growth and analysis. K.W. and T.T. acknowledge support from the Elemental Strategy Initiative conducted by the MEXT, Japan, grant number JPMXP0112101001, JSPS KAKENHI grant number JP20H00354 and the CREST(JPMJCR15F3), JST for bulk hBN crystal growth and analysis. E.C.R. acknowledges support from the Department of Defense (DoD) through the National Defense Science & Engineering Graduate Fellowship (NDSEG) Program. S.L. acknowledges support from Kavli ENSI Heising Simons Junior Fellowship. M.H.N. thanks S. Kundu and M. Jain for their implementation of noncollinear wavefunction plotting in Siesta. Computational resources were provided by Cori at National Energy Research Scientific Computing Center (NERSC), which is supported by the Office of Science of the US Department of Energy under contract no. DE-AC02-05CH11231, Stampede2 at the Texas Advanced Computing Center (TACC) through Extreme Science and Engineering Discovery Environment (XSEDE), which is supported by National Science Foundation under grant no. ACI-1053575 and Frontera at TACC, which is supported by the National Science Foundation under grant no. OAC-1818253.

Author contributions

M.F.C., F.W. and S.L. conceived the project, and S.G.L. supervised the theoretical calculations. H.L. and S.L. performed the STM measurements, and M.H.N. carried out the DFT and GW calculations. H.L., J.X., X.L., J.W., W.Z., S.Z. and S.K. fabricated the heterostructure device. E.R. and D.W. performed the second harmonic generation measurements. K.Y., M.B. and S.T. grew WSe_2 and WS_2 crystals. K.W. and T.T. grew the hBN single crystal. All authors discussed the results and wrote the manuscript.

Competing interests

The authors declare no competing interests.

Additional information

Supplementary information The online version contains supplementary material available at https://doi.org/10.1038/s41563-021-00923-6.

Correspondence and requests for materials should be addressed to S.L., S.G.L., F.W. or M.F.C.

Peer review information *Nature Materials* thanks Andrea Young and the other, anonymous, reviewer(s) for their contribution to the peer review of this work.

Reprints and permissions information is available at www.nature.com/reprints.